

## Article

# Preparation of Cerium Oxide via Microwave Heating: Research on Effect of Temperature Field on Particles

Chao Lv <sup>1,\*</sup> , Hong-Xin Yin <sup>1</sup>, Yan-Long Liu <sup>1</sup>, Xu-Xin Chen <sup>1</sup>, Ming-He Sun <sup>1</sup> and Hong-Liang Zhao <sup>2,\*</sup> 

<sup>1</sup> School of Control Engineering, Northeastern University, Qinhuangdao 066004, China; 2072123@stu.neu.edu.cn (H.-X.Y.); 2172254@stu.neu.edu.cn (Y.-L.L.); 2172245@stu.neu.edu.cn (X.-X.C.); 1971722@stu.neu.edu.cn (M.-H.S.)

<sup>2</sup> School of Metallurgical and Ecological Engineering, University of Science and Technology Beijing, Beijing 100083, China

\* Correspondence: lvchao@neuq.edu.cn (C.L.); zhaohl@ustb.edu.cn (H.-L.Z.)

**Abstract:** Micro–nano cerium oxide particles with regular morphology and good dispersity have been widely used in polishing and other industrial fields. Microwave heating is an effective, controllable and green heating technology. The Venturi reactor used for microwave heating developed by our team was the core equipment utilized to study the effects of pyrolysis conditions on the purity and microstructure of cerium oxide particles. The experiments were carried out and the products were characterized using XRD, SEM and EDS. Microwave heating, fluid flow and chemical reaction were coupled using numerical simulation, the effects of microwave power, reactor location and waveguide arrangement on temperature fields were investigated. The results showed that with the microwave power increasing, the degree of crystallinity and purity of cerium oxide improved. The morphology gradually became sphere-like. Varied reactor locations and waveguide arrangements changed the gradient and dispersity of temperature fields. Bulk particles and agglomeration could be avoided, and cerium oxide particles with average size of 80 nm were produced when the reactor was located in the center of the cavity. Vertical arrangement of waveguides had the advantages of higher temperature value, gentle gradient and better dispersity.

**Keywords:** microwave heating; cerium oxide; temperature field; morphology



**Citation:** Lv, C.; Yin, H.-X.; Liu, Y.-L.; Chen, X.-X.; Sun, M.-H.; Zhao, H.-L. Preparation of Cerium Oxide via Microwave Heating: Research on Effect of Temperature Field on Particles. *Crystals* **2022**, *12*, 843. <https://doi.org/10.3390/cryst12060843>

Academic Editors: Alessandra Toncelli and Željka Antić

Received: 11 May 2022

Accepted: 10 June 2022

Published: 15 June 2022

**Publisher's Note:** MDPI stays neutral with regard to jurisdictional claims in published maps and institutional affiliations.



**Copyright:** © 2022 by the authors. Licensee MDPI, Basel, Switzerland. This article is an open access article distributed under the terms and conditions of the Creative Commons Attribution (CC BY) license (<https://creativecommons.org/licenses/by/4.0/>).

## 1. Introduction

Cerium oxide ( $\text{CeO}_2$ ) is a cost-effective rare earth oxide that can be utilized in multiple applications.  $\text{CeO}_2$  has been widely used in industrial applications, including chemical–mechanical polishing, fuel cells and catalyzers [1–4]. In recent years, the preparation method of  $\text{CeO}_2$  has been extensively investigated. L. Xiang [5] prepared micro–nano  $\text{CeO}_2$  by the static roasting of  $\text{CeCl}_3$ . The purity of  $\text{CeO}_2$  increased when the roasting temperature increased. However, a serious agglomeration of particles appeared in this method. This was because the conventional heating method had a significant temperature gradient, which was not of benefit for obtaining a good morphology of particles [6]. Microwaves are electromagnetic waves of which wavelength ranges from 1 mm to 1 m. When an ion solution is heated, polar molecules and ions move intensely and crash into each other, which contributes to the heat release [7]. Microwave heating has the advantages of accelerating the chemical reaction rate [8,9], selective heating [10,11] and easy control. H. Chen [12] used zirconyl chloride octahydrate ( $\text{ZrOCl}_2 \cdot 8\text{H}_2\text{O}$ ) and ammonia water ( $\text{NH}_3 \cdot \text{H}_2\text{O}$ ) as raw materials to prepare nanometer zirconium dioxide ( $\text{ZrO}_2$ ) via the coprecipitation–conventional heating method and the coprecipitation–microwave pyrolysis method. It was found that the  $\text{ZrO}_2$  prepared using the conventional heating method had the disadvantages of uneven particle size and agglomeration, the size of the  $\text{ZrO}_2$  particles exceeded 60 nm. The particles prepared using microwave heating had better dispersity, of which size was less 40 nm.

During experiments of microwave heating, chemical reaction process cannot be observed because of the non-transparent equipment, therefore numerical simulation has become an essential tool to predict and visualize the temperature field [13–16]. S. Yu et al. [17] investigated the pyrolysis process of methyl ricinoleate using microwave-assisted heating. The effects of waveguide quantity and heating power in pyrolysis process were studied. It was found that higher energy efficiency was obtained at higher power. The waveguide quantity had much influence on the electric field distribution; however, no obvious difference on temperature distribution was observed. J. Zhu et al. [18] coupled electromagnetism and heat by computing the Maxwell's equations, wave equation and heat transfer equation. The effects of microwave power on the temperature field of oil shale were investigated using numerical simulation. The selective characteristic of microwave heating was beneficial to the porosity and permeability enhancement of the sample. Higher microwave power contributed to higher temperature, which increased the heating efficiency. The above studies demonstrated that both microwave powers and waveguides had significant effects on the intensity and distribution of electromagnetic field.

In this study, different temperature fields were obtained when microwave power, reactor location and waveguide distribution were changed. Then, both experiment and numerical simulation were carried out to investigate the influence of different temperature fields on purity and morphology of products.

## 2. Experimental

The schematic diagram of the experiment was shown in Figure 1. Oxygen bottles provided oxygen for the chemical reaction. Oxygen velocity was measured using the gas flow meter.  $\text{CeCl}_3$  solution was prepared by the  $\text{CeCl}_3 \cdot 7\text{H}_2\text{O}$  (99%, analytical grade, Sinopharm Chemical Reagent Co., Ltd., Shanghai, China). It was jetted into the Venturi reactor, which was developed by our team, the droplets were collided into smaller droplets by high-speed oxygen. These droplets mixed well with oxygen due to an increased contact area with oxygen, which accelerated the chemical reaction. In the industrial production process of pyrolysis method, HCl was used to dissolve or recycle rare earth ore in the process of extraction separation. However, there were no conditions for HCl recovery in the laboratory. Therefore, the gas produced by the reaction was absorbed by the  $\text{Na}_2\text{CO}_3$  solution.

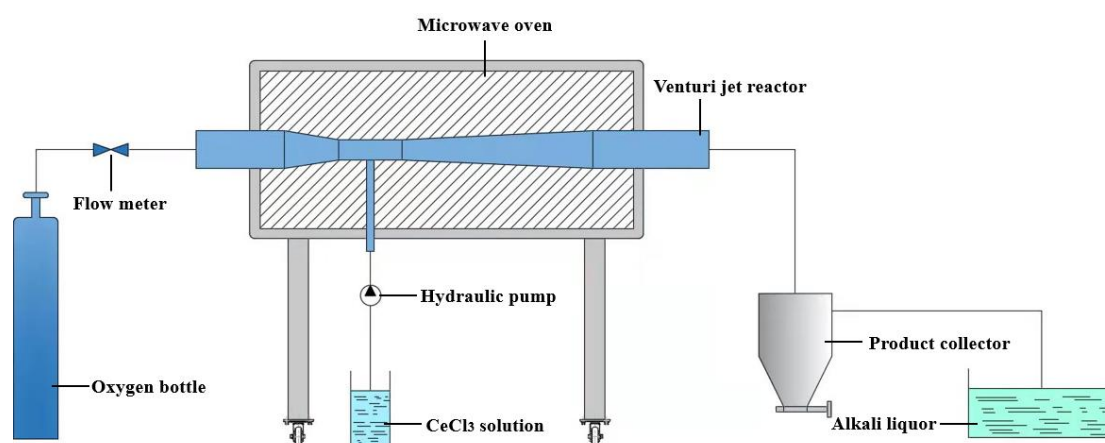


Figure 1. Schematic diagram of the experiment.

The phase composition of the products was determined using X-ray diffraction (XRD, Empyrean S3, PANalytical, Mumbai, India) at a scanning rate of  $5^\circ/\text{min}$  in the  $2\theta$  range from  $10^\circ$  to  $90^\circ$  with  $\text{Cu K}\alpha$  radiation ( $\lambda = 1.540598 \text{ nm}$ ). The microstructure of particles was observed using scanning electron microscopy (SEM, apreo2c, Thermo Fisher, Waltham, MA, USA). The average content of residual chlorine element was measured using energy dispersive spectroscopy (EDS, ultim max 40, Oxford, UK).

### 3. Numerical Simulation

#### 3.1. Geometry

According to the microwave oven used in the experiment (custom-made by the Shan-Lang Experimental Material Management Department), the simplified three-dimensional model was shown in Figure 2. Three rectangular BJ26 waveguides were equidistantly distributed on the surface of the microwave cavity. Dimensions of the microwave oven and Venturi tube were shown in Table 1.

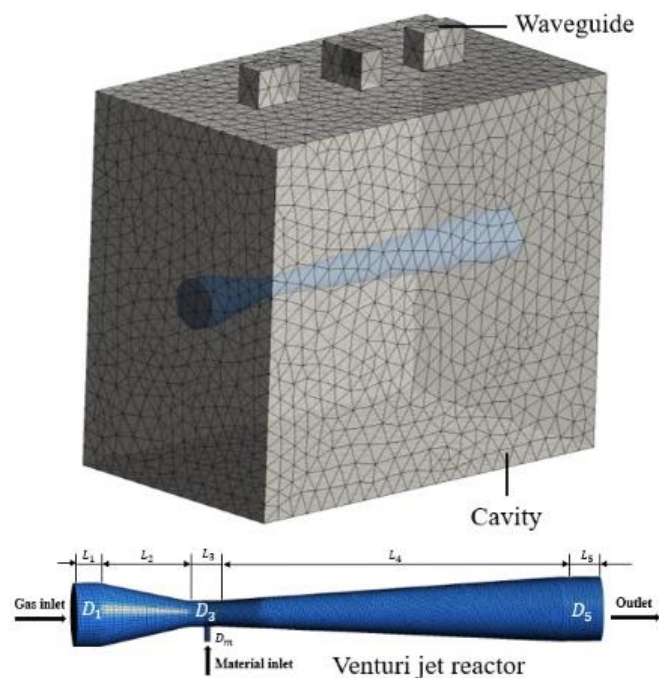


Figure 2. Simplified three-dimensional model of the equipment.

Table 1. Dimensions of models.

	Length/mm	Width/mm	Height/mm	Diameter/mm
Cavity	690	400	600	-
Waveguide	86.36	43.18	60	-
L1	-	-	30	-
L2	-	-	110	-
L3	-	-	40	-
L4	-	-	419	-
L5	-	-	50	-
D1	-	-	-	80
D3	-	-	-	32
D5	-	-	-	80
Dm	-	-	-	7

#### 3.2. Governing Equation

The electromagnetic field inside the Venturi reactor is determined using the Maxwell’s equation. The time-varying form of the Maxwell’s equations can be expressed in the form below:

$$\nabla \cdot \mathbf{D} = \rho_e \tag{1}$$

$$\nabla \cdot \mathbf{B} = 0 \tag{2}$$

$$\nabla \times \mathbf{E} = -\frac{\partial \mathbf{B}}{\partial t} \tag{3}$$

$$\nabla \times \mathbf{H} = -\frac{\partial \mathbf{D}}{\partial t} + \mathbf{J} \tag{4}$$

where  $B$  is the magnetic flux density ( $\text{Wb}/\text{m}^3$ ),  $D$  is the electric displacement or electric flux density ( $\text{C}/\text{m}^2$ ),  $E$  is the electric field intensity ( $\text{V}/\text{m}$ ),  $H$  is the magnetic field intensity ( $\text{A}/\text{m}$ ),  $J$  is the current density ( $\text{A}/\text{m}^2$ ) and  $\rho_e$  is the electric charge density ( $\text{C}/\text{m}^3$ ).

The complex relative permittivity,  $(\epsilon_r)$ , is defined as:

$$\epsilon_r = \epsilon' - j\epsilon'' \quad (5)$$

where  $j = \sqrt{-1}$ ,  $\epsilon'$  is the dielectric constant and  $\epsilon''$  is the corresponding loss factor (that is, the imaginary part of the dielectric constant).  $\epsilon'$  represents the ability of microwaves to penetrate the material, while  $\epsilon''$  represents the ability of the material to store electricity.

The differential wave equation deduced using Maxwell's equations was used to describe the electromagnetic field distribution:

$$\nabla \times \mu_r^{-1}(\nabla \times E) - k_0^2 \left( \epsilon_r - \frac{j\sigma}{\omega\epsilon_0} \right) E = 0 \quad (6)$$

$$k_0 = \omega/c_0 \quad (7)$$

where  $\omega$  is the angular frequency ( $\text{rad}/\text{s}$ ),  $\epsilon_0$  is the free space permittivity ( $8.85 \times 10^{-12} \text{ F}/\text{m}$ ),  $\mu_r$  is the relative permeability,  $\sigma$  represents the electrical conductivity ( $\text{S}/\text{m}$ ),  $k_0$  is the wave number in free space and  $c_0$  represents the speed of light in vacuum ( $\text{m}/\text{s}$ ).

When the electromagnetic field interacts with the solution, part of the electromagnetic energy transforms into thermal energy, which is the source item of the energy equation. The energy absorbed by the per unit volume solution can be expressed using the following equation:

$$Q = \frac{1}{2} \omega \epsilon_0 \epsilon'' |E|^2 \quad (8)$$

where  $|E|$  is the electric field modulus.

The energy equation is given as:

$$\frac{\partial(\rho T)}{\partial t} + \nabla \cdot (v\rho T) = \nabla \cdot \left( \frac{k}{c_p} \nabla T \right) + Q \quad (9)$$

where  $T$  represents the temperature ( $^\circ\text{C}$ ),  $k$  is the thermal conductivity [ $\text{W}/(\text{m}\cdot\text{K})$ ],  $\rho$  is the density of the fluid,  $c_p$  represents the specific heat capacity,  $v$  is the velocity and  $Q$  is the source item.

The chemical reaction occurring inside the Venturi reactor can be expressed as:



In the reactor, every relative species needs to observe the species mass conservation equation:

$$\frac{\partial(\rho Y_i)}{\partial t} + \nabla \cdot (\rho v Y_i) = -\nabla J_i + R_i + S_i \quad (11)$$

where  $Y_i$  is the mass fraction of the  $i$ th substance,  $R_i$  is the net produce rate of the chemical reaction of the  $i$ th substance,  $S_i$  is the discrete phase of the  $i$ th substance that is responsible for the additional produce rate caused by the user-defined source item and  $J_i$  is the diffusive flux of the  $i$ th substance produced by the concentration gradient.

### 3.3. Material and Boundary Conditions

The main physical parameters, including permittivity, conductivity, thermal conductivity, specific heat and density, were measured in this study. The measured results of the parameters were shown in Table 2. Enthalpy, entropy and other necessary parameters were determined from the Practical Inorganic Thermodynamics Data Manual [19].

**Table 2.** Main physical parameters measured at 363 K.

Properties	Dielectric Constant	Loss Factor	Electrical Conductivity	Thermal Conductivity	Specific Heat	Density
Symbol	$\epsilon'$	$\epsilon''$	$\sigma$	$k$	$C_p$	$\rho$
Value	80.49	0.785	0.1383 S/m	0.53 W/(m·K)	5.025 J/(g·K)	1.023 g/cm <sup>3</sup>
Function	$T$	$T$	$T$	$T$	$T$	-
Source	This study	This study	This study	This study	This study	This study

Where  $\epsilon' = 0.0003T^2 - 0.006T + 46.535$ ,  $\epsilon'' = -0.0011T^2 + 0.9937T - 151.307$ ,  $\sigma = 3.29 \times 10^{-5}T^2 - 0.0197T + 2.9515$ ,  $k = -1.06 \times 10^{-5}T^2 + 0.0081T - 1.0261$ ,  $C_p = 2.87 \times 10^{-5}T^2 - 0.016T + 7.043$ . The density did not change much when the temperature changed.

To decrease the difficulty associated with the simulation and the computing period, the following assumptions were proposed before solving the mathematical models:

1. Microwave frequency is constant (2.45 GHz).
2. The initial temperature inside the reactor is uniform (25 °C).
3. The fluid inside the reactor is incompressible.
4. Permeability is constant at 1.

The boundary conditions of the model were shown in Table 3. Three-dimensional transient algorithm was selected in the Fluent 19.0 software. The following models were used for the simulation: Eulerian multiphase, standard k- $\epsilon$  turbulence, energy equation and species transport models. Pressure and velocity were coupled using the SIMPLE algorithm. The computations were considered to converge when the residuals for all the quantities did not exceed more than  $10^{-3}$ , except for energy equation with the residual below  $10^{-6}$ .

**Table 3.** Boundary conditions.

	Boundary Type	Value
Excitation	Wave port	-
Wall of waveguides and cavity	Perfect E boundary	-
Gas velocity	Velocity-inlet	7 m/s
Material velocity	Velocity-inlet	0.2 m/s
Outlet	Outflow	-

### 3.4. Independence Verification of Grid

The whole model was composed of unstructured grids. A local coordinate system and an influence sphere were built at the Venturi tube, which contributed to the local encrypted grids. The average quality of the grids was 0.842. Independence verification of grids is shown in Figure 3. When the quantity of the grids reached 410 K, the error of the temperature value at outlet was less than 10 K, which indicated that the grid quantity did not cause too much fluctuation of the simulated results. To raise the simulated efficiency, grid quantity of 410 K was used in this study.

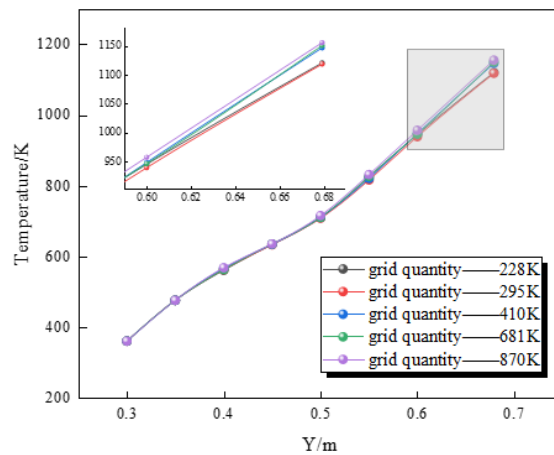


**Figure 3.** Independence verification of the grid.

## 4. Results and Discussion

### 4.1. Effect of Microwave Power

The experiment and simulation were both carried out when microwave power was 12, 13, 14, 15 and 16 kW, respectively. The comparison of  $\text{Cl}^-$  content of the product between experiment and simulation was shown in Figure 4. The error was below 3% (the error bar in Figure 4 was 3%). It proved that the used model, parameters and boundary conditions were rational.  $\text{Cl}^-$  content was less than 2% when the power reached 16 kW. The inserted XRD pattern showed that a single phase  $\text{CeO}_2$  was obtained when the power reached 14 kW. The increased power caused higher strength of the diffraction peaks. The software, MDI Jade, and the method of multipeak separation were used to analyze the degree of crystallinity of products at each diffraction peak. As for the products prepared at 16 kW, the degree of crystallinity at the diffraction peak at  $2\theta = 28.56^\circ$ ,  $56.383^\circ$  and  $59.097^\circ$  was obviously higher than that prepared at 14 kW. The degree of crystallinity at the other diffraction peaks was almost equal under the two microwave powers. It indicated that higher microwave power was beneficial to the improvement of the degree of crystallinity.

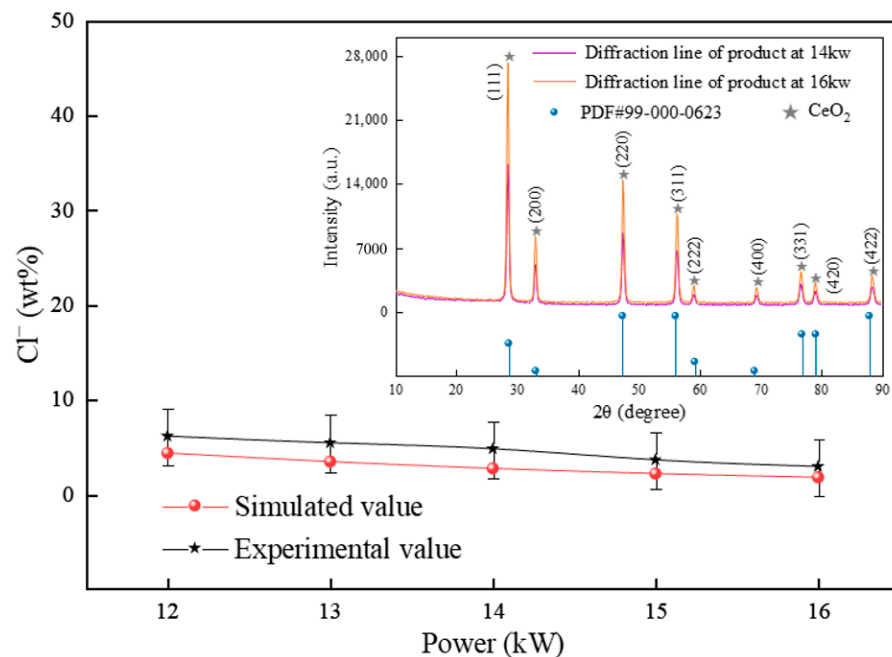


**Figure 4.** Comparison of  $\text{Cl}^-$  content between experiment and simulation.

The comparison of SEM images was shown in Figure 5.  $\text{CeO}_2$  particles had a sharp morphology when it was produced at 14 kW. The increased power led to higher temperature. Sphere-like particles were obtained when power reached 16 kW. It indicated that the higher microwave power was beneficial to the improvement of the particles' morphology.

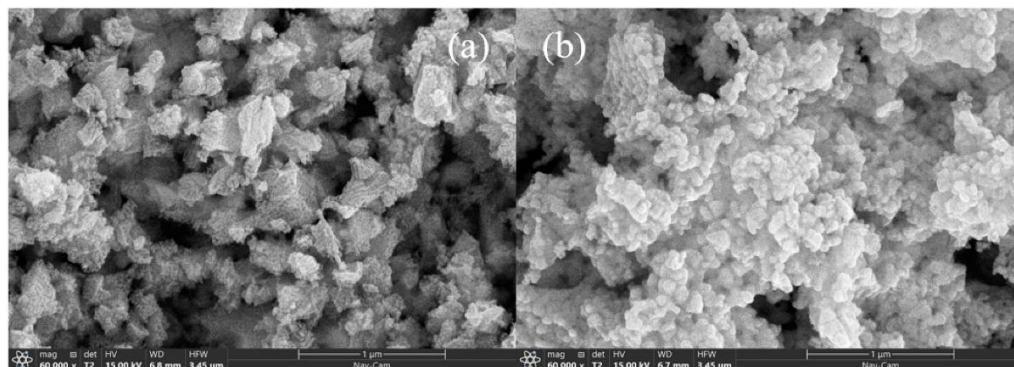


Figure 5. SEM images. (a) 14 kW, (b) 16 kW.

#### 4.2. Effects of Reactor Location

Different reactor locations led to variations in the electromagnetic and temperature fields inside the reactor. The schemes were shown in Figure 6a. The simulated temperature fields at 12 kW were shown in Figure 6b. Temperature value was higher in the center than it was when closer to the wall, which accorded with the features of the microwave heating model. With the reactor location changing, temperature fields varied considerably. However, the model of center heating was not changed. The temperature value was always 300 K in the front part of the reactor because only oxygen existed there, which is a substance that cannot absorb microwaves.

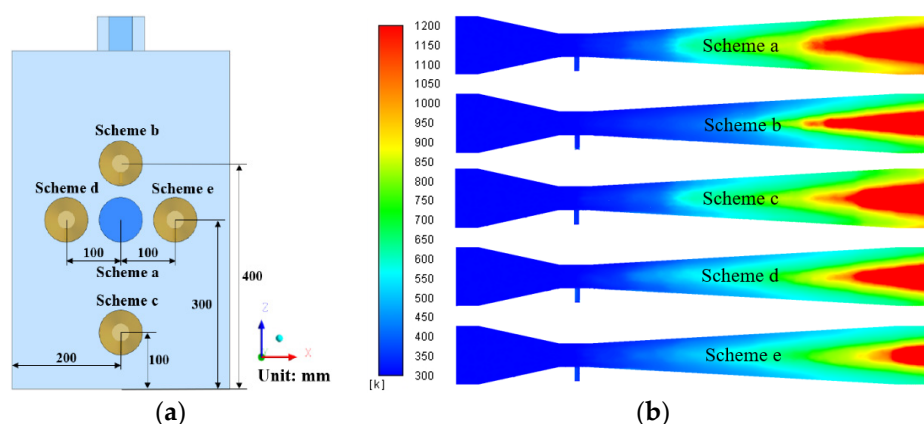
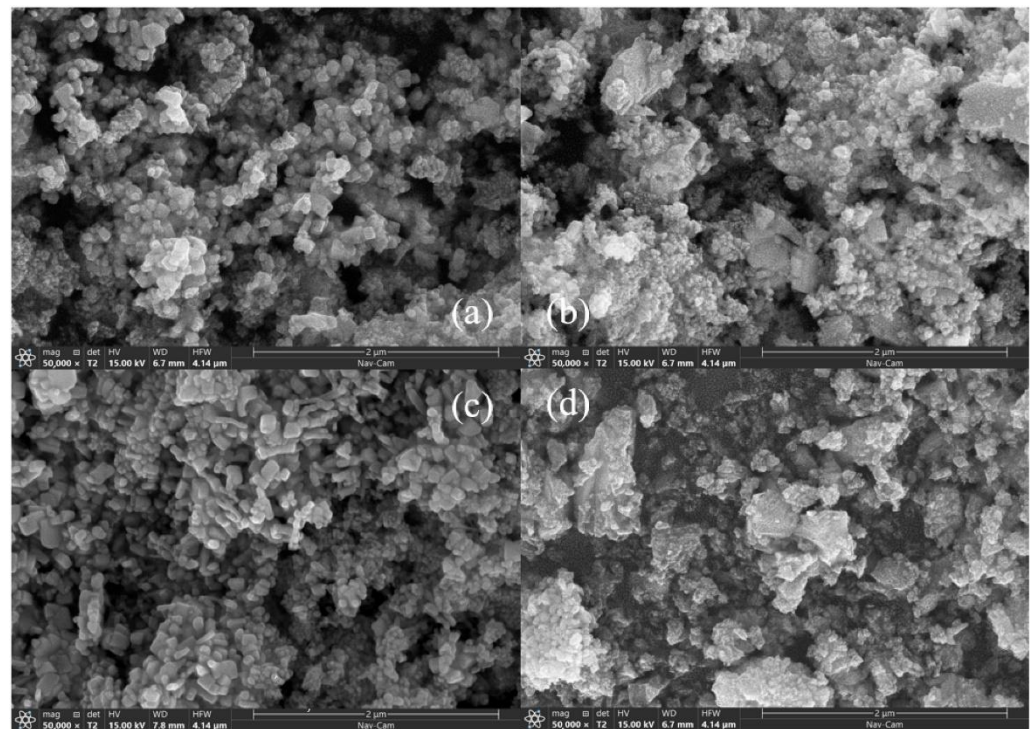


Figure 6. (a) Schemes of different reactor locations, (b) temperature field.

Scheme (a) shows the highest average temperature and the gentlest temperature gradient in the radial direction. Scheme (b) shows the worst temperature dispersity in the axial direction because the region of high temperature was concentrated at the end of the reactor. The temperature dispersity of Scheme (d) was better than Scheme (b), which benefited the reactant as it was heated earlier. Scheme (e) had the worst temperature field distribution because there was a significant radial temperature gradient and the lowest average temperature. It is obvious that the temperature field of Scheme (c) was similar to Scheme (a). Therefore, the products of Schemes (a), (b), (d) and (e) were characterized using SEM, as shown in Figure 7. The  $\text{CeO}_2$  particles produced via Scheme (a) had a regular morphology and its average particle size was near 80 nm, the smallest among the four Schemes. However, each single particle produced via Scheme (b) had a crude morphology, which may be attributed to the shortened heating time of the solution caused

by the concentrative temperature field. Additionally, it had a bad particle dispersity.  $\text{CeO}_2$  produced via Scheme (d) had a relative regular morphology, even particle size and good dispersity. In Figure 7d, it is obvious that serious agglomeration and many bulk particles appeared. According to the above results, it can be concluded that a gentler temperature gradient was beneficial for eliminating the agglomeration and bulk particles. Comparing the simulated temperature fields and SEM images of Scheme (b) with (d), it was found that a better temperature dispersity contributed to a better dispersity of particles.



**Figure 7.** SEM images. (a) Scheme (a), (b) Scheme (b), (c) Scheme (d) and (d) Scheme (e).

#### 4.3. Effects of Waveguide Distribution

The effect of various waveguide distributions on the temperature field was investigated. Numerical simulation was used to predict the morphology and purity of the products due to the high cost of experimental equipment. Differently to the experimental Scheme, three new Schemes of waveguide arrangements and their temperature fields were shown in Figure 8. All the Schemes had a good axial temperature dispersity. However, in Scheme (a), the waveguides were parallelly arranged and had an extremely large temperature gradient at the end of the reactor, and the temperature at most regions was below 600 K, which may not cause the chemical reaction. The vertically arranged waveguides of Schemes (b) and (c) led to higher than average temperature values and gentler temperature gradients. Based on the former deductions and the SEM images of the experiment, as seen in Scheme (a), it can be predicted that there is a high probability that the agglomeration and bulk particles will appear and, for each particle, that sharp morphology will appear. Comparing the temperature fields of Scheme (b) and (c) with the experimental field, it can be deduced that the phenomenon of agglomeration is unlikely to appear because of the gentle temperature gradient and that  $\text{CeO}_2$  particles produced via Scheme (b) will have a more regular morphology than Scheme (c). Figure 9 showed the temperature and  $\text{Cl}^-$  content at the outlet of the three new Schemes.  $\text{Cl}^-$  content reached 16.85% due to the low overall temperature of Scheme (a). It can be predicted that the  $\text{Cl}^-$  content of  $\text{CeO}_2$  produced by Scheme (b) will be close to 2.07%.

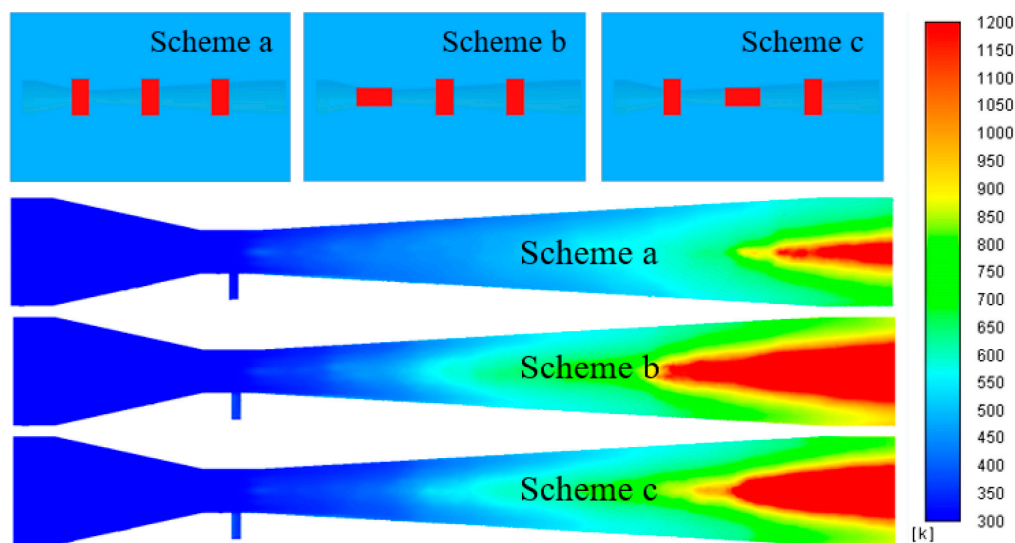


Figure 8. Schemes of waveguide distributions and their temperature fields.

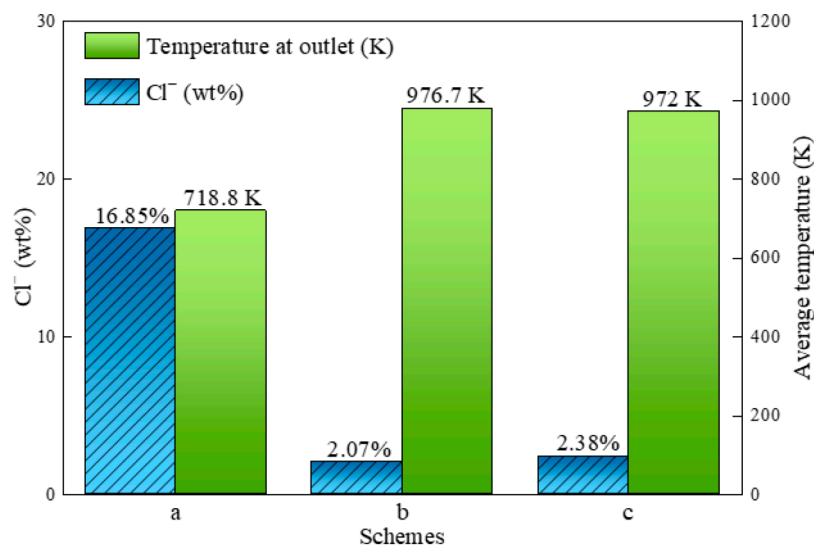


Figure 9. Comparison of temperature at outlet and Cl<sup>-</sup> content.

## 5. Conclusions

In this study, the effects of microwave power, reactor location and waveguide distribution on the CeO<sub>2</sub> purity and microstructure were investigated. The following conclusions were obtained:

1. Microwave power had significant effects on the purity of the products. Higher power contributed to higher purity and an improvement of the degree of crystallinity of CeO<sub>2</sub>. When microwave power reached 16 kW, sphere-like CeO<sub>2</sub> particles were obtained and the residual Cl<sup>-</sup> content was only 0.15%. Increasing microwave power also had benefits for obtaining a more regular morphology of particles.
2. Various reactor locations caused various temperature fields to present varied temperature gradients and dispersities, which had a remarkable effect on the microstructure of CeO<sub>2</sub> particles. The simulated nephogram of temperature fields combined with SEM images showed that large temperature gradients caused agglomeration and bulk particles to appear, and better temperature dispersity contributed to a better dispersity of particles. When the reactor was located in the center of the cavity, CeO<sub>2</sub> particles with a regular morphology were prepared, which had an average size of 80 nm.

3. Varied waveguide arrangements also caused various temperature fields. The vertical arrangement of waveguides had the advantages of higher temperature value, gentle gradient and better dispersity. It was predicted that the actual value of  $\text{Cl}^-$  content was close to 2.07% when the waveguides were distributed in Scheme (b). Moreover, the morphology was similar to Scheme (c) and better than Scheme (a).

From the perspective of energy efficiency, at the current stage, there is a problem of high energy consumption. Reducing energy consumption and improving the energy utilization while ensuring the product quality will be the focus in the next stage of study. In addition, gas velocity determined the atomization effect, which can change the microstructure of the particles. In the next stage, the effect of gas velocity on particle microstructure will be worth studying.

**Author Contributions:** Conceptualization, C.L.; Project administration, C.L.; Funding acquisition, C.L.; Methodology, C.L. and H.-X.Y.; Software, H.-X.Y.; Validation, Y.-L.L. and X.-X.C.; Data Curation, M.-H.S.; Visualization, H.-L.Z. All authors have read and agreed to the published version of the manuscript.

**Funding:** This research was supported by the National Natural Science Foundation of China (51904069), the Natural Science Foundation of Hebei Province of China (E2019501085), the Fundamental Research Funds for the Central Universities (N2223026), the Scientific Research Fund Project of Northeastern University at Qinhuangdao (XNY201808).

**Institutional Review Board Statement:** Not applicable.

**Informed Consent Statement:** Not applicable.

**Data Availability Statement:** Not applicable.

**Conflicts of Interest:** The authors declare no conflict of interest.

## References

1. Fujiwara, A.; Yoshida, H. In-Situ diffuse reflectance spectroscopy analysis of Pd/CeO<sub>2</sub>-ZrO<sub>2</sub> model three-way catalysts under Lean-Rich cycling condition. *Catal. Today* **2021**, *376*, 269–275. [[CrossRef](#)]
2. Chen, Y.S.; Fan, J. Synthesis of high stability nanosized Rh/CeO<sub>2</sub>-ZrO<sub>2</sub> three-way automotive catalysts by Rh chemical state regulation. *J. Energy Inst.* **2020**, *93*, 2325–2333. [[CrossRef](#)]
3. Fan, J.; Chen, Y.S. A simple and effective method to synthesize Pt/CeO<sub>2</sub> three-way catalysts with high activity and hydrothermal stability. *J. Environ. Chem. Eng.* **2020**, *8*, 104236. [[CrossRef](#)]
4. Jiang, D.; Wan, G. Elucidation of the Active Sites in Single-Atom Pd<sub>1</sub>/CeO<sub>2</sub> Catalysts for Low-Temperature CO Oxidation. *ACS Catal.* **2020**, *10*, 11356–11364. [[CrossRef](#)]
5. Xiang, L. Study on the Preparation of Light Rare Earth Oxide from Rare Earth Chloride Roasted Statically. Master's Thesis, Northeastern University, Shenyang, China, 2010.
6. Li, H.; Xu, J.L. Food waste pyrolysis by traditional heating and microwave heating: A review. *Fuel* **2022**, *324*, 124574. [[CrossRef](#)]
7. Arballo, J.R.; Goni, S.M. Modeling of fluid dynamics and water vapor transport in microwave ovens—ScienceDirect. *Food Bioprod. Process.* **2020**, *119*, 75–87. [[CrossRef](#)]
8. Wang, B.; Zheng, H.B. Microwave-assisted fast pyrolysis of waste tires: Effect of microwave power on products composition and quality. *J. Anal. Appl. Pyrolysis* **2021**, *155*, 104979.
9. Zhou, N.; Dai, L.L. Catalytic pyrolysis of plastic wastes in a continuous microwave assisted pyrolysis system for fuel production. *Chem. Eng. J.* **2021**, *418*, 129412. [[CrossRef](#)]
10. Luo, W.; Huang, S.Y. Three-dimensional mesostructure model of coupled electromagnetic and heat transfer for microwave heating on steel slag asphalt mixtures. *Constr. Build. Mater.* **2022**, *330*, 127235. [[CrossRef](#)]
11. Shen, X.; Li, H. Imaging of liquid temperature distribution during microwave heating via thermochromic metal organic frameworks. *Int. J. Heat Mass Transfer.* **2022**, *189*, 122667. [[CrossRef](#)]
12. Chen, H. Study on Preparation and Mechanism of Yttria-Stabilized Zirconia Nanosized Powder by Microwave Pyrolysis. Master's Thesis, Zhengzhou University, Zhengzhou, China, 2014.
13. Sadeghi, A.; Hassanzadeh, H. Thermal analysis of high frequency electromagnetic heating of lossy porous media. *Chem. Eng. Sci.* **2017**, *172*, 13–22. [[CrossRef](#)]
14. Lv, C.; Sun, M.H. Pyrolysis Preparation Process of CeO<sub>2</sub> with the Addition of Citric Acid: A Fundamental Study. *Crystals* **2021**, *11*, 912. [[CrossRef](#)]
15. Xu, T.; Song, G. Visualization and simulation of steel metallurgy processes. *Int. J. Miner. Metall. Mater.* **2021**, *28*, 1387–1396. [[CrossRef](#)]

16. Yuan, F.; Xu, A.J. Development of an improved CBR model for predicting steel temperature in ladle furnace refining. *J. Miner. Metall. Mater.* **2021**, *28*, 1321–1331. [[CrossRef](#)]
17. Yu, S.Z.; Duan, Y. Three-dimensional simulation of a novel microwave-assisted heating device for methyl ricinoleate pyrolysis. *Appl. Therm. Eng.* **2019**, *153*, 341–351. [[CrossRef](#)]
18. Zhu, J.Y.; Yi, L.P. Three-dimensional numerical simulation on the thermal response of oil shale subjected to microwave heating. *Chem. Eng. J.* **2021**, *407*, 127197. [[CrossRef](#)]
19. Ye, D.L. *Practical Inorganic Thermodynamics Data Manual*; Cao, S.L., Ed.; Metallurgical Industry Press: Beijing, China, 1981; pp. 262–263, 265–266.